ASH SINTERING IN THE PRESENCE

OF A CO_2-H_2O VAPOR

by

ERIN COLLEEN HOXSIE

A THESIS

Presented to the Department of Earth Sciences
and the Graduate School of the University of Oregon
in partial fulfillment of the requirements
for the degree of
Master of Science

June 2018

THESIS APPROVAL PAGE

Student: Erin Colleen Hoxsie

Title: Ash Sintering in the Presence of a CO_2-H_2O Vapor

This thesis has been accepted and approved in partial fulfillment of the requirements for the Master of Science degree in the Department of Earth Sciences by:

Mark Reed	Chairperson
Thomas Giachetti	Member
James Watkins	Member

and

Sara D. Hodges   Interim Vice Provost and Dean of the Graduate School

Original approval signatures are on file with the University of Oregon Graduate School.

Degree awarded June 2018

THESIS ABSTRACT

Erin Colleen Hoxsie

Master of Science

Department of Earth Sciences

June 2018

Title: Ash Sintering in the Presence of a CO_2-H_2O Vapor

We carried out rhyolite ash sintering experiments in the presence of a mixed CO_2-H_2O vapor using both fine and coarse ash. Fine ash is barely sintered after 7 minutes and fully densified after about 30 minutes. Coarse ash is barely sintered after 45 minutes and fully densified after a few hours. Vesicle relaxation from initially angular shapes to spherical shapes takes longer than estimated from scaling relations. The experimental sintering and vesicle relaxation timescales substantiate the hypothesis that natural obsidian pyroclasts from Mono Craters, California (USA) form by ash sintering. Two observations are interpreted as the most direct evidence yet that CO_2 flushing from a deeper magmatic was involved in the eruption: (1) the preservation of sharp-tipped vesicles in domains of clasts that have high dissolved CO_2 concentrations, and (2) the anticorrelation between H_2O and CO_2 observed in multiple clasts.

This thesis includes previously unpublished co-authored material.

CURRICULUM VITAE

NAME OF AUTHOR: Erin Colleen Hoxsie

GRADUATE AND UNDERGRADUATE SCHOOLS ATTENDED:

University of Oregon, Eugene
Sonoma State University, Rohnert Park, California

DEGREES AWARDED:

Master of Science, Geological Sciences, 2018, University of Oregon
Bachelor of Science, Geology, 2011, Sonoma State University

AREAS OF SPECIAL INTEREST:

Geochemistry
Volcanology

PROFESSIONAL EXPERIENCE:

Graduate Employee, University of Oregon, 2016-2018

Exploration Geologist, North American Palladium, 2011-2013

GRANTS, AWARDS, AND HONORS:

Outstanding Student Award, Association for Women Geoscientists, 2011

G. Davidson Woodard Scholarship, Sonoma State University, 2011

Student Research Grant, Sonoma County Uplift, Sonoma State University, 2010

ACKNOWLEDGMENTS

TABLE OF CONTENTS

LIST OF FIGURES

LIST OF TABLES

CHAPTER I

OVERVIEW

The body of this thesis is original research prepared for submission to *Bulletin of Volcanology* with Dr. James Watkins, Dr. Thomas Giachetti, and Dr. James Gardner as coauthors.

Dr. Gardner collaborated on ash sintering experiments at the University of Texas: Austin. Dr. Watkins and Dr. Giachetti contributed editorial support throughout. Dr. Watkins contributed assistance with experimental set-ups and original material to the discussion section. The rest of the work presented is my own.

CHAPTER II

ASH SINTERING IN THE PRESENCE

OF A CO_2-H_2O VAPOR

Material in this chapter is being prepared for publication with Dr. James Watkins, Dr. Thomas Giachetti, and Dr. James Gardner.

I. Introduction

Ash clouds are a distinguishing feature of explosive volcanic eruptions. They originate from conduits where a bubbly magmatic mixture undergoes fragmentation and transitions to a gas-particle flow (Dufek et al., 2012). Above the fragmentation depth, collisions produce fine particles and ash, and given sufficient time, ash particles that are hot and/or wet enough can sinter together to form larger particles or pyroclasts along conduit walls (Gardner et al., 2017; Watkins et al., 2017). As ash sinters, volcanic gas is trapped to form irregular-shaped, sharp-tipped vesicles that over time relax to a spherical shape. Vesicle formation in this way is distinct from vapor exsolution from a volatile oversaturated melt, and must be considered when interpreting the textural characteristics of vesicles as well as the concentration of dissolved volatiles retrieved from volcanic pyroclasts.

New evidence suggest that obsidian pyroclasts in volcanic tephra deposits form by ash sintering (Gardner et al., 2017; Watkins et al., 2017) as opposed to other mechanisms, such as cooling of melt along conduit margins (Newman et al., 1988; Rust et al., 2004; Rust and Cashman, 2007) or collapse of permeable magmatic foam (Eichelberger et al., 1986). The pyroclast shown in Fig. 1, for example, has multiple domains that are separated by dark bands riddled with broken xenocrysts and rock fragments. This dark material is not found within co-genetic pumice, and hence, foam collapse is not consistent with the distribution of this material (Gardner et al., 2017). Some parts of the clast house elongate vesicles (Figs. 1b and 1c) whose irregular shapes can be ascribed to gas trapped between ash particles that underwent sintering and shear deformation. Area maps of dissolved H_2O and CO_2 (Figs. 1d and 1e) reveal steep chemical gradients that, based on diffusion modeling, could have originated no more than a few hours before erupting (Watkins et al., 2017). This timescale

2

is orders of magnitude shorter than the experimentally-detrived timescale for foam collapse of viscous rhyolite (Martel and Iacono-Marziano, 2015). Collectively, these observations point to ash sintering for trapping magmatic gases and preserving a record of gas-melt exchange in volcanic conduits.
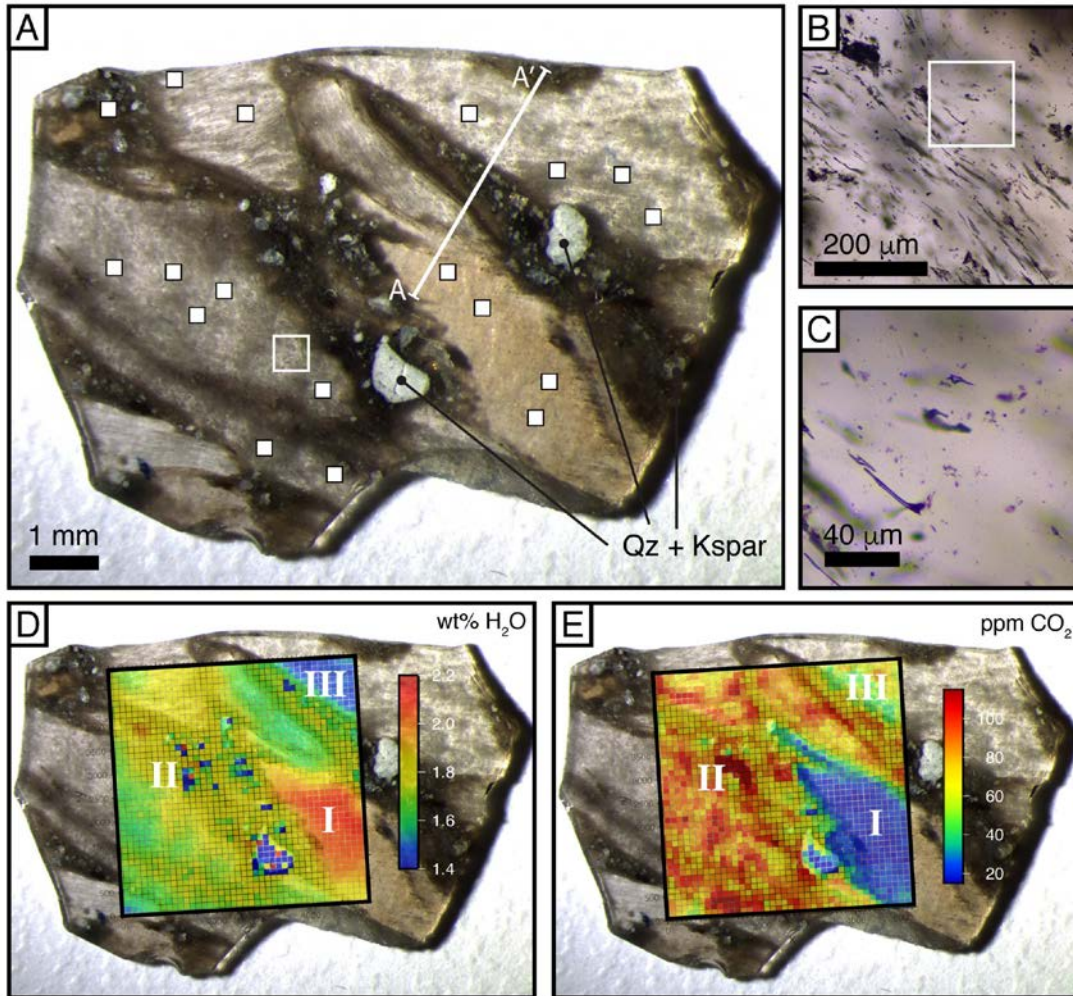
Figure 1. (a) Obsidian pyroclast from Mono Craters, CA (USA). The clast exhibits multiple textural domains that are interpreted to have formed by sintering in the conduit prior to the eruptive quench. Squares show locations of electron microprobe measurements of major element composition. The white box shows the field of view in (b), and the white line shows the location of a high-resolution transect of H_2O and CO_2 measurements. Panels (b) and (c) are transmitted light images showing the sharp-tipped, elongate vesicles seen within the clast. (d) Dissolved H_2O measured by FTIR is relatively homogenous throughout much of the clast (domain II) except for a domain with low H_2O (domain III) and a domain with high H_2O (domain I). (e) Dissolved CO_2 is heterogeneous throughout much of the clast, except for a domain with intermediate concentration (III) and a domain with low concentration (I).

Although hot ash is involved in all pyroclastic eruptions, few experimental investigations on the evolution of vapor and melt during ash sintering have been carried out. An exception is a recent study by Gardner et al. (2018), in which natural rhyolite ash was sintered in the presence of a pure H_2O fluid. They showed that an initially porous, unconsolidated coarse ash formed a dense, H_2O-saturated obsidian within a few minutes at 800ºC or about 20 minutes at 750ºC. The inferred timescales for H_2O diffusion, ash sintering, and vesicle relaxation were used to estimate how long ash-filled cracks could remain open as permeable pathways for magma outgassing (Castro et al., 2014; Gardner et al., 2017). Here, we expand upon the experiments of Gardner et al. (2018) by studying ash sintering in the presence of a mixed H_2O-CO_2 fluid. The addition of CO_2 is important because it affects the solubility of water, and therefore the melt viscosity. Slow diffusion of CO_2 can thus be a rate-limiting factor in the time evolution of porosity, vapor composition, and melt rheology, which leads us to pose the following questions addressed herein:

1. How does the presence of CO_2 affect ash sintering time and the evolution of porosity?
2. How do vapor bubbles affect the measurement of dissolved volatile concentrations?
3. How can experimentally sintered ash inform the interpretation of textures and chemical gradients seen in natural obsidian pyroclasts?

II. Methods

Sintering experiments of various durations were carried out at 800ºC and 40 MPa. These conditions overlap the run conditions of sintering experiments by Gardner et al. (2018) and are in the range of conditions recorded by the Mono Craters magmas (Carmichael et al., 1966; Newman et al., 1988).

2.1 Glass synthesis

For starting material, we used microlite-free and bubble-free obsidian prepared by F.J. Ryerson at Lawrence Livermore National Laboratory. The glass was made by mixing reagent-grade oxide powders in proportions designed to match the composition of the 1340 A.D. Mono Craters obsidian flows based on Table 2 in Newman et al. (1988). The powder

was mixed in an automated mortar and pestle, placed in an Al_2O_3 crucible, dried under a heat lamp, and then fused in a bottom-loaded, one-atmosphere Deltech furnace at 1600ºC. The mixture was allowed to cool from 1600 to 650ºC and held overnight to anneal the internal stresses. The furnace was then turned off the and the sample cooled to 150ºC in about 5 hours (Ryerson, pers. comm.). This yielded a relatively large batch of anhydrous, microlite- and bubble-free rhyolite glass for experiments.
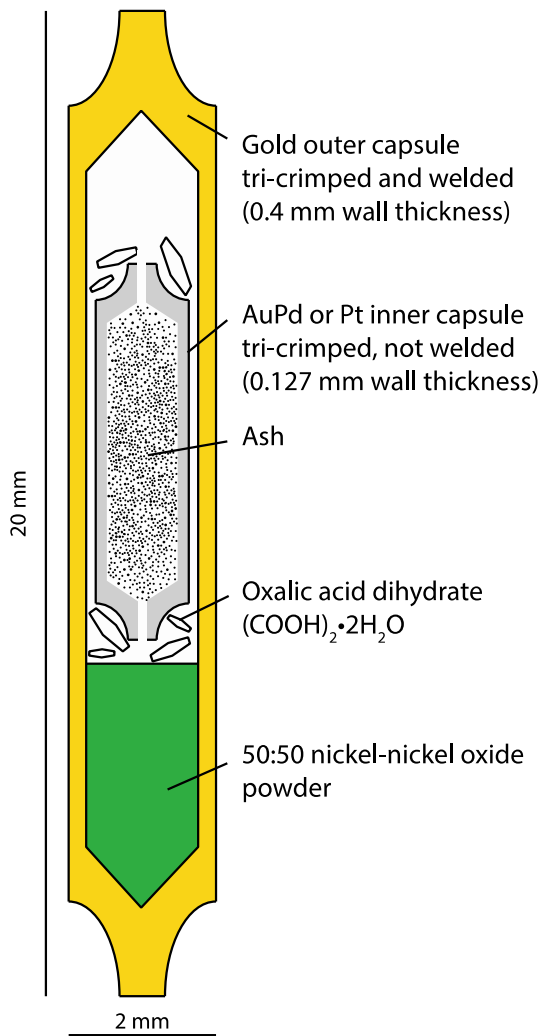
The glass was crushed, sieved, and ash particle size was measured with a PartAn^{3D} particle size analyzer. The PartAn^{3D} tracks particles as they fall off a vibrating conveyor belt. The machine takes multiple 2D images of each particle and finds the average width, length, and thickness of the particle to calculate volume. The PartAn^{3D} can measure particles ranging in size from ~50 microns to ~35 millimeters by analyzing 100 images per second with a high-speed, high-resolution camera.

2.2 Ash sintering experiments

A schematic of the double-capsule experimental assembly used is shown in Fig. 2. Approximately 15-20 mg of ash were poured into a 10 mm long Au-Pd capsule (2 mm outer diameter) that was tri-crimped but not welded, allowing the CO_2-H_2O vapor to permeate the ash particles. The outer capsule was loaded with a 50:50 mixture of nickel and nickel oxide (NNO) and oxalic acid dehydrate (OAD; $(COOH)_2 \cdot 2H_2O$). The purpose of the NNO is to buffer the oxygen fugacity and control the composition of the vapor produced by decomposition of OAD at the run conditions (Yoshimura and Nakamura, 2010). Decomposition of OAD produces a vapor that is ~60 mol% CO_2 and 40 mol% H_2O (see below). The amount of OAD used was ~15-30% by weight of the ash to ensure vapor saturation.

Experiments were run using a computer-controlled, rapid-quench cold-seal pressure vessel (CSPV). The loaded capsules were placed in an Inconel cylinder, which was then inserted into a pressure vessel. The pressure vessel was connected to a pressure line and H_2O was used as the pressure medium. The sample remained inside a water-cooled jacket while the pressure vessel was heated to the desired temperature, as measured by a type K thermocouple. Temperature did not vary by more than ±2°C. Pressure was measured by a pressure transducer precise to ±0.1 MPa. Once the pressure vessel reached the desired

5

temperature, the sample was raised into the hot zone of the vessel using an external magnet. Pressure dropped by ~20 MPa when the sample was raised, but was readjusted to the setpoint within 30 seconds. During the run, pressure oscillated by 0.5 MPa. To end an experiment, the magnet was lowered, bringing the sample into the water-cooled jacket to achieve as rapid a quench as possible. When the sample was lowered, pressure increased by ~20 MPa but was readjusted within 30 seconds.

Figure 2. Schematic of the experimental double-capsule design for ash sintering experiments.

Gold outer capsule tri-crimped and welded (0.4 mm wall thickness)

AuPd or Pt inner capsule tri-crimped, not welded (0.127 mm wall thickness)

Ash

Oxalic acid dihydrate $(COOH)_2 \cdot 2H_2O$

50:50 nickel-nickel oxide powder

20 mm

2 mm

2.3 FTIR measurements

Post-run capsules were cut with a diamond saw and mounted in epoxy and then ground with 400 grit silicon carbide paper to expose the sample surface. The surface was polished using progressively higher grit paper followed by 3 μm and 1 μm diamond paste. The

6

polished sample was mounted on a glass slide using Crystalbond[TM] and sectioned to a thickness of about 1 mm using a diamond wafer saw. The sample was ground to a thickness of 300 to 500 μm and the polishing procedure was repeated. Doubly-polished wafers were removed from the glass slide either with acetone or heat, cleansed of Crystalbond[TM] with acetone, and then transferred to an aluminum sample holder for analysis by transmission Fourier Transform Infrared (FTIR) spectroscopy.

Measurements of OH, H_2O_m, OH, and CO_2 concentrations were made using a Thermo Nicolet Nexus 670 FTIR spectrometer. Absorbance measurements were made using a 15x objective, infrared source, MCT-A detector and KBr beamsplitter. We typically use a 100 μm aperture, step size of 100 μm, spectral resolution of 4 cm^{-1}, 64 scans per spot, and 64 scans for the background, which is collected every 10 minutes. Conversion of absorbance to concentration is based on the Beer-Lambert law:

$$C_i = \frac{M_i \cdot Abs}{\varepsilon \rho d} \tag{1}$$

where M_i is the molecular weight (g mol^{-1}1^{-1}), Abs is the absorbance (peak height minus linear baseline), ρ is the sample density (~2380 g L^{-1} for rhyolite glass; Newman et al., 1986), d is the thickness of the wafer (cm), and ε is the molar absorption coefficient (L cm^{-1} mol^{-1}). We converted absorbances to concentrations for H_2O using expressions from Zhang et al. (1997) and for CO_2 using expressions from Behrens et al. (2004). The thickness of wafers was measured using a digital caliper with 1 µm precision before and after the sample was removed from the glass slide. This led to the realization that a thin layer (~30-50 μm) of CrystalBond[TM] separates the sample wafer from the glass slide and can lead to erroneous thickness measurements if samples are measured prior to removal from the glass slide.

When converting a measured absorbance to concentration using Eq. 1, we assume that the quantities in the denominator (absorption coefficient, density, and thickness) are constant despite the presence of crystals and vesicles. The influence of these factors on the reported concentrations is assessed on a sample-by-sample basis as discussed further below.

2.4 Synchrotron FTIR measurements

Several high-resolution transects and area maps were made on the natural pyroclast by synchrotron FTIR at the Advanced Light Source. We present results from one of these transects (location shown in Fig. 1) that runs across all three domains identified in the area maps. The main advantage of synchrotron FTIR is that the spatial resolution is diffraction limited and the spot size is about 5 μm, whereas in conventional FTIR, we use a square aperture with 100 μm dimensions.

2.5 Electron microprobe measurements

Major element compositions were analyzed for one natural pyroclast (locations shown in Fig. 1a) on a Cameca SX-100 electron microprobe (EPMA) using a 15 kV accelerating voltage and a 10 nA beam current (50 nA for Cl, F, S, and Ti). A beam size of 10 μm was used for all analyses. Na, K, Si, and Al were measured first, and their concentrations were calculated using a time-dependent intensity correction. The results show a remarkable homogeneity in major element composition between the different textural domains of the clast (Table 1).

	Domain I (n=4)	Domain II (n=10)	Domain III (n=4)	Newman et al. (1988)
SiO_2	73.70 (0.58)	73.96 (0.46)	74.15 (0.56)	76.45 (0.73)
Al_2O_3	13.12 (0.17)	13.26 (0.17)	13.19 (0.13)	12.32 (0.20)
CaO	0.53 (0.01)	0.54 (0.01)	0.55 (0.02)	0.52 (0.02)
MgO	0.03 (0.01)	0.03 (0.01)	0.03 (0.01)	0.01 (0.01)
FeO*	1.01 (0.02)	0.99 (0.02)	1.00 (0.02)	1.02 (0.04)
TiO_2	0.05 (0.01)	0.06 (0.01)	0.06 (0.004)	0.059 (0.009)
Na_2O	3.98 (0.06)	3.85 (0.06)	4.03 (0.07)	3.8 (0.15)
K_2O	4.63 (0.02)	4.66 (0.03)	4.68 (0.03)	4.75 (0.07)
MnO	0.03 (0.02)	0.03 (0.01)	0.04 (0.01)	0.06 (0.03)
Total	97.10	97.38	97.73	98.99

Table 1: Major element composition of the three domains of the pyroclast as measured by electron microprobe (standard deviation). The three domains are homogeneous and in good agreement with the composition of Mono Craters obsidian reported by Newman et al. (1988).

2.6 Vesicularity measurements

Two-dimensional digital image analysis was used to quantify porosity. High-resolution photomicrogaphs were taken of the samples using a Leica DMC4500 camera mounted on a Leica DM2700 microscope. Vesicle identification was carried out using Adobe Photoshop software. Assuming the samples are isotropic, the vesicle content (ϕ, in vol%) and bubble shape/circularity were measured in two dimensions using Image-J software.

## III. Results

3.1 Sintering experiments

Since the time evolution of vesicle shapes and porosity is expected to depend on particle size as well as melt viscosity, we conducted two sets of experiments, one using "fine ash" and one using "coarse ash" (Fig. 3).
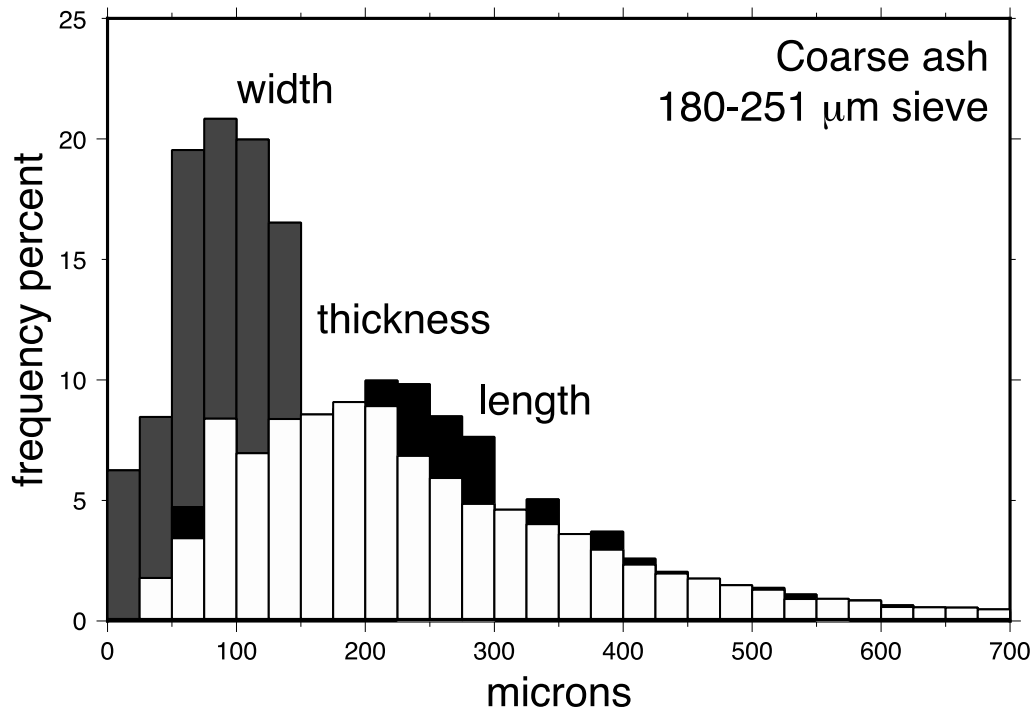
Figure 3. Particle sizes used in coarse ash sintering experiments.

For fine ash, after 7 minutes of sintering the porosity has decreased from ~40% initially (cf. Gardner et al., 2018) to 15% but the vesicles have retained their initial irregular shapes with sharp tips. Shorter duration experiments were not attempted because the 7 minute run was barely sintered enough to make into a doubly polished thin section. After 15 minutes of sintering, the porosity has decreased further to $\phi = 8.6\%$, and the smaller bubbles have relaxed to a nearly spherical shape while the larger vesicles remain subrounded and deformed. After 30 minutes, the porosity is only slightly lower at $\phi = 6.8\%$, but most vesicles, large and small, have relaxed to nearly spherical shapes (Fig. 4, top row).

In our coarse ash experiments, a similar textural evolution takes place but over a longer period of time. After 45 minutes, the ash is barely sintered and the vesicles have irregular, high aspect ratio shapes. After 7 hours, the porosity has decreased to $\phi = 8\%$ and some high aspect ratio vesicles are still present. After 24 hours, the ash is fully sintered and densified ($\phi < 1\%$) and there are only a few spherical vesicles (Fig. 4, bottom row).
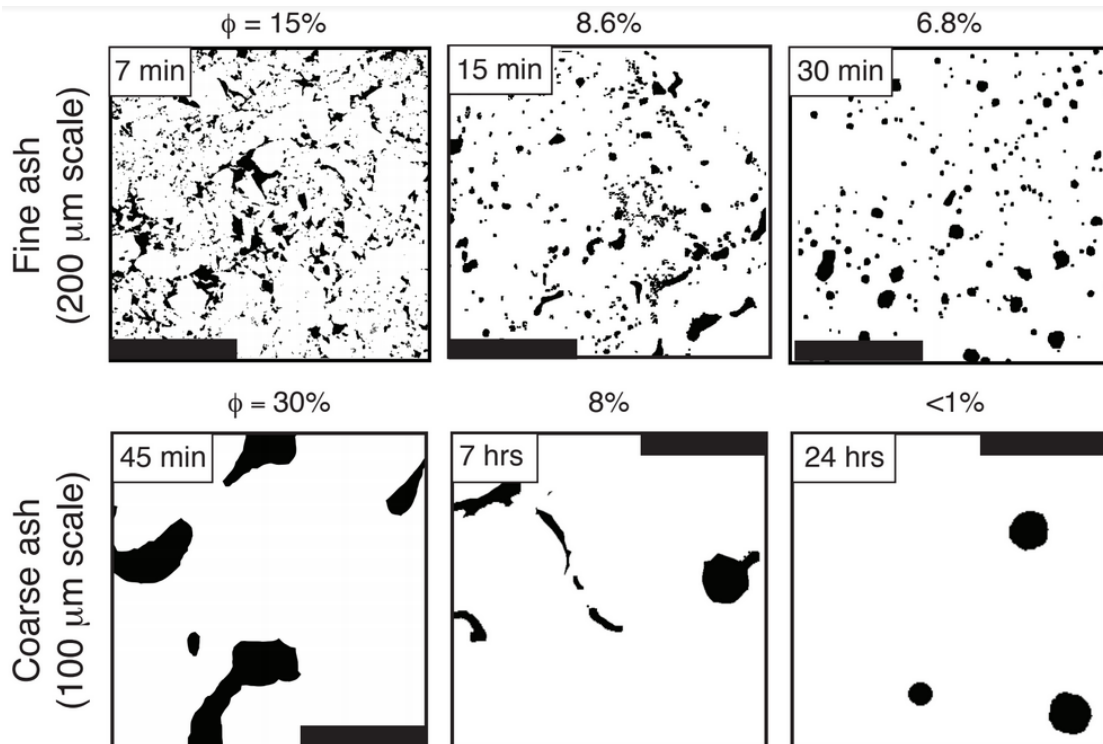

Figure 4. Textural evolution during sintering of fine ash (top row) and coarse ash (bottom row). Dark spots are vesicles. The panels were made by processing reflected light photomicrographs in Photoshop and ImageJ. Porosities were determined from the entire thin sections and not necessarily from the panel areas shown.

3.2 Dissolved volatiles

The dissolved volatile contents of the glasses vary systematically with run duration in both sets of experiments (Figs. 5a-b). The longer runs (15 and 30 minutes for fine ash, 7 and 24 hours for coarse ash) plot on or near the 40 MPa isobar on a CO_2 vs. H_2O plot - a strong indication that these run durations are sufficient to establish vapor-melt equilibrium. By contrast, data from shorter runs are well below the isobar, either because vapor-melt equilibrium has not been established or because of analytical artifacts caused by higher porosities.

Water speciation is used to calculate a cooling rate (Q) for each of the samples (Figs. 5c-d). The hydrous species cooling rate speedometer is based on the homogeneous interconversion reaction between molecular H_2O species and OH species in silicate melts and glasses, and can be applied to infer cooling rates of hydrous rhyolitic glasses (Zhang et al., 2000). The longer runs yield the highest cooling rates of ~100 to 1000 K/s, which is hereafter taken to be the "known" rapid quench rate of the experimental assembly. This cooling rate range agrees with previously published values by Zhang et al. (2000) in their original calibration. By contrast, the shorter duration runs yield cooling rates that are anomalously low. These low values amount to higher H_2O_m/OH ratios and are thus likely artifacts related to the infrared beam intersecting H_2O-bearing vesicles, as discussed by Gardner et al. (2018).
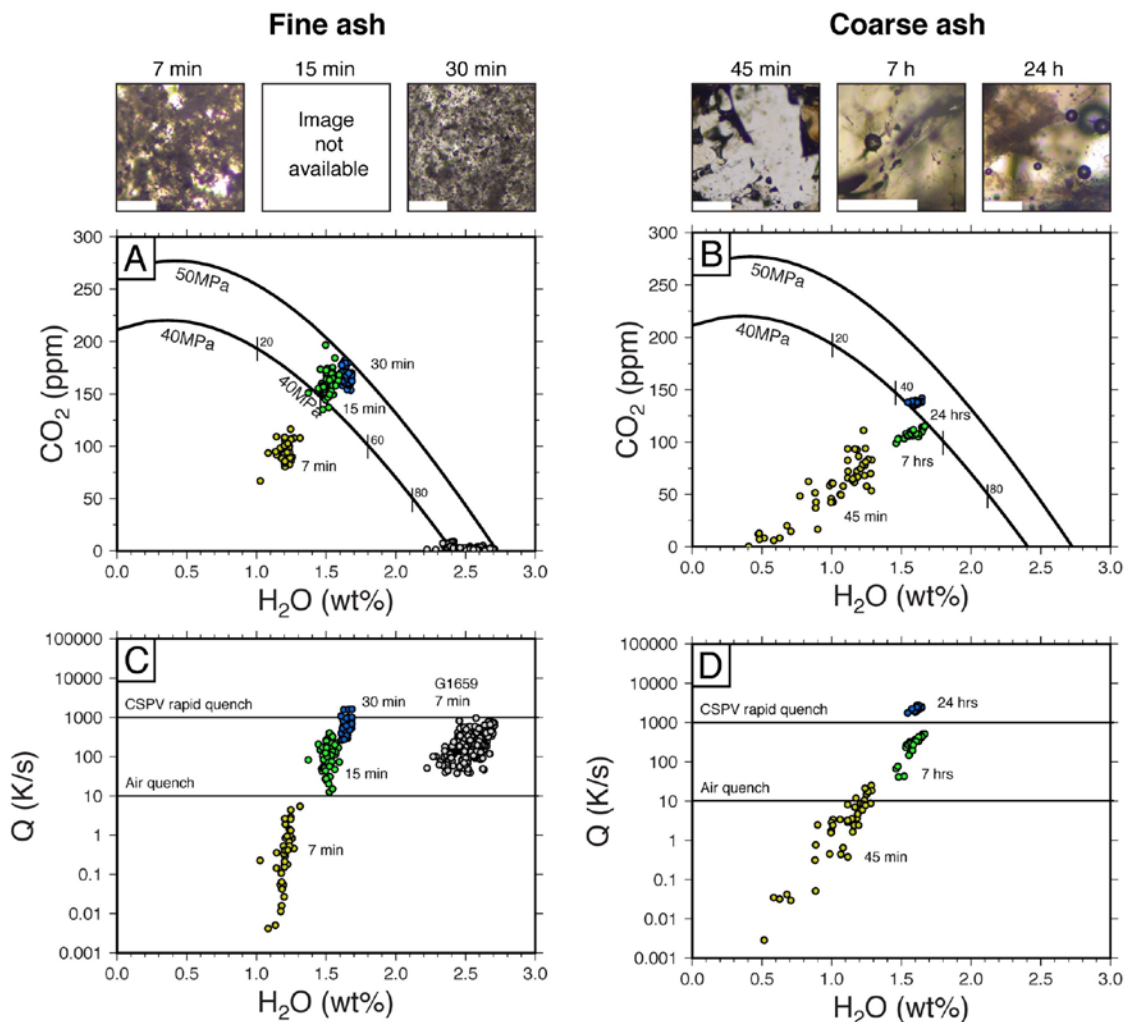
Figure 5. Volatile concentrations from sintering experiments using fine and coarse ash. Top panels show transmitted light images of the run products (scale bar = 200 μm). Panels (a) and (b): As run duration increases, the data plot closer to the 40 MPa isobar. Panels (c) and (d): Melt cooling rates based on H_2O_m/OH ratios. Samples with low vesicularity yield realistic cooling rates of 100-1000 K/s. Anomalously low values (less than about 50 K/s) can be attributed to excess absorbance from H_2O_m housed in vesicles, and are thus an artifact of the transmission FTIR measurements.

IV. Discussion

4.1 The effect of CO_2 on ash sintering time and the evolution of porosity

The details of ash sintering at the pore scale depend on the geometry and rheology of particle-particle contacts and can thus be quite complicated (Wadsworth et al., 2014). It is nevertheless useful to frame the discussion in terms of a simple scaling relationship, where the timescale for sintering is written as (Gardner et al., 2017):

$$\tau_s \sim \frac{\eta \, L}{\sigma} \qquad (2)$$

where η (Pa s) is melt viscosity, σ (N m^{-1}) is surface tension, and L (m) is a characteristic length scale, which is the particle radius, in the case of incipient sintering, or inter-particle pore radius, in the case of thorough sintering (Wadsworth et al., 2016). Here, we assume σ = 0.22 N m^{-1} (Bagdassarov et al., 2000), and focus our attention on melt viscosity and particle size.

Our fine ash experiments are similar to the unsieved experiments of Gardner et al. (2018) because of similar particle size range (1 to 10's of microns) and because sintering takes place in a regime where the ash can be assumed to be fully hydrated because the timescale for water diffusion into the cores of 10 micron ash particles is only about 1 minute at 800˚C. The presence of CO_2 lowers the solubility of water from 2.4 wt% to about 1.5 wt%, which increases melt viscosity from $\log_{10}\eta$ = 6.1 to 6.8 (Hess and Dingwell, 1996). Figure 6 shows the importance of viscosity on the textural evolution of fine ash as empirically determined by Gardner et al. (2018). The textural evolution of our fine ash is in general agreement with the results of Gardner et al. (2018), though our ash seems to undergo densification slightly faster, presumably because our ash has a greater proportion of finer particles.
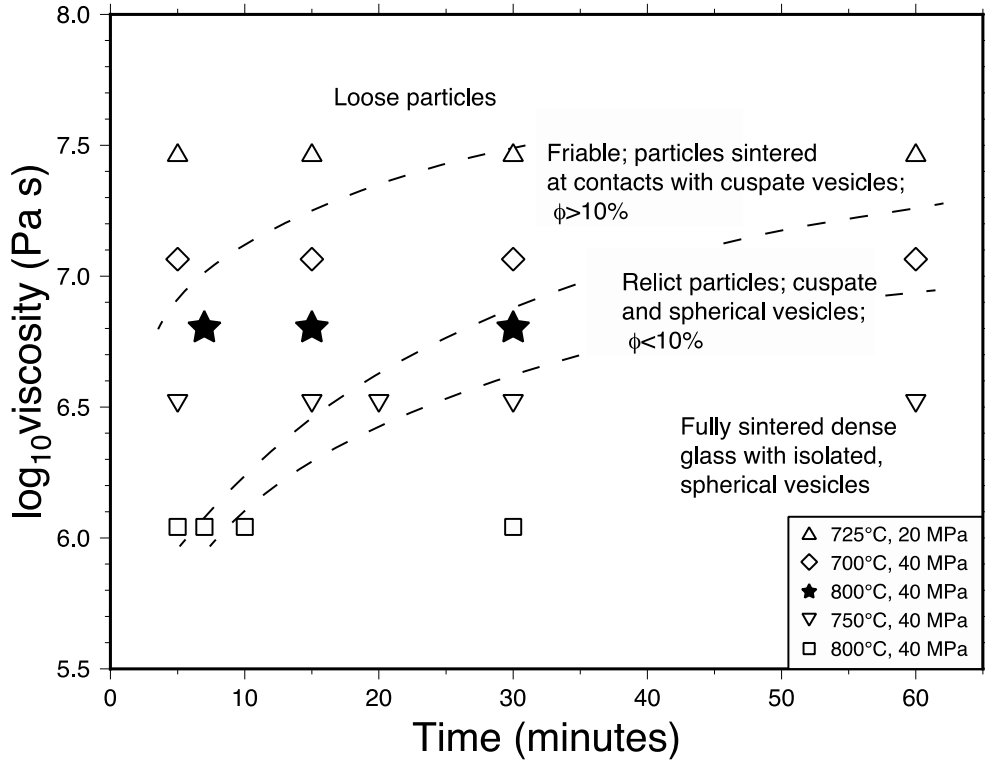
Figure 6. Regime diagram modified from Gardner et al. (2018) showing the time evolution of textures during sintering as a function of melt viscosity and run duration. Open symbols show results from Gardner et al. (2018) at 700-800°C and 20-40 MPa. Closed symbols are results from this study at 800°C and 40 MPa, which yield textures that are in general agreement with the regimes defined by Gardner et al. (2018). Ash sintering takes longer at 725°C and 20 MPa than 700°C and 40 MPa because of the lower solubility of water at 20 MPa.

Our coarse ash experiments are similar to the sieved experiments of Gardner et al. (2018) study because of similar particle sizes on the order of 100 microns. Like their experiments, the ash in our coarse experiments sinters in a regime where the melt is not expected to be fully hydrated throughout the run because it takes longer than one hour for water to diffuse into the cores of 100 micron particles. Hence, the relevant melt viscosity is somewhere between that of a dry melt ($\eta \sim 10^9$-10^{10}) and a water-saturated rhyolitic melt ($\eta \sim 10^7$). This explains why the sintering and vesicle relaxation processes are prolonged to tens of minutes to hours when coarse particles are involved.

*4.2 The effect of vapor bubbles on the measurement of dissolved volatile concentrations*

Our experiments provide an opportunity to quantify how CO_2-rich vapor bubbles affect the conversion of a measured absorbance to concentration using Eq. 1. The presence of vesicles can lower the effective thickness of the glass wafer, lower the average density of the sample being analyzed, and change the molar absorption coefficient in unknown ways (von Aulock et al., 2014). Hence it is important to question whether H_2Om and CO_2 in vesicles lead to anomalously low or high dissolved volatile concentrations. The first conclusion to draw is that absorbance measurements are not significantly affected by vesicle-related artifacts in the 30-minute run despite a relatively high porosity ($\phi = 6.8\%$); the CO_2-H_2O data plot in a tight cluster around the 40 MPa isobar (Fig. 5a) and yield the correct, "known" cooling rate from the rapidly quenched experiments (Fig. 5c). The shorter 15-minute run has a higher porosity ($\phi = 8.6\%$), but the data still plot on or near the 40 MPa isobar. However, the calculated cooling rates are lower, reflecting a higher H_2O_m/OH ratio, suggesting that 8.6% porosity can yield small but noticeable artifacts. The 7-minute run, which has the highest porosity of the three samples ($\phi = 15\%$), shows similar artifacts as the 15-minute run but magnified. Based on these results, we conclude that low porosities ($\phi < 10\%$) are desirable for obtaining meaningful dissolved H_2O and CO_2 concentration measurements and that anomalously low cooling rates can be discarded from data sets. We also conclude that volatile species in vesicles lead to underestimated cooling rates and tend to shift the measured concentrations to lower values for both H_2O and CO_2 – an indication that the cause of the analytical artifacts is changes in the effective thickness of the sample wafers as opposed to infrared absorption by gaseous H_2O and CO_2.

4.3 Comparison between experimentally sintered ash and natural obsidian pyroclasts

The sintering experiments we carried out were motivated by observations made on obsidian pyroclasts from Mono Craters, California (Watkins et al., 2017). The pyroclast shown in Fig. 1 is not particularly unusual and it exemplifies three behaviors documented in other pyroclasts from the same eruption (Fig. 7). First, the area surrounding Domain I shows an anti-correlation between H_2O and CO_2 where H_2O and CO_2 are counter-diffusing. A CO_2-H_2O anti-correlation was seen in data from several other pyroclasts (red, orange, green and purple fields of Fig. 7), but those clasts did not preserve such clear contextual

15

information; i.e., CO_2-H_2O counter-diffusion from the juxtaposition of two parcels of melt that have nearly or partially equilibrated with different vapor compositions. Second, Domains II and III show high CO_2 variability at fixed H_2O content. This was seen in one clast previously (teal field in Fig. 7), and in both clasts where this occurs, we observe cuspate, sharp-tipped vesicles. Third, intraclast gradients in dissolved H_2O are relatively smoothed out whereas those for CO_2 are not. In this section, we use the pyroclast from Fig. 1 to show how timescales for melt cooling, vesicle relaxation, ash sintering, and H_2O-CO_2 diffusion are archived within pyroclasts, and how they can be used more generally as a window into pyroclast formation and the nature of vapor-melt exchange during magma ascent.
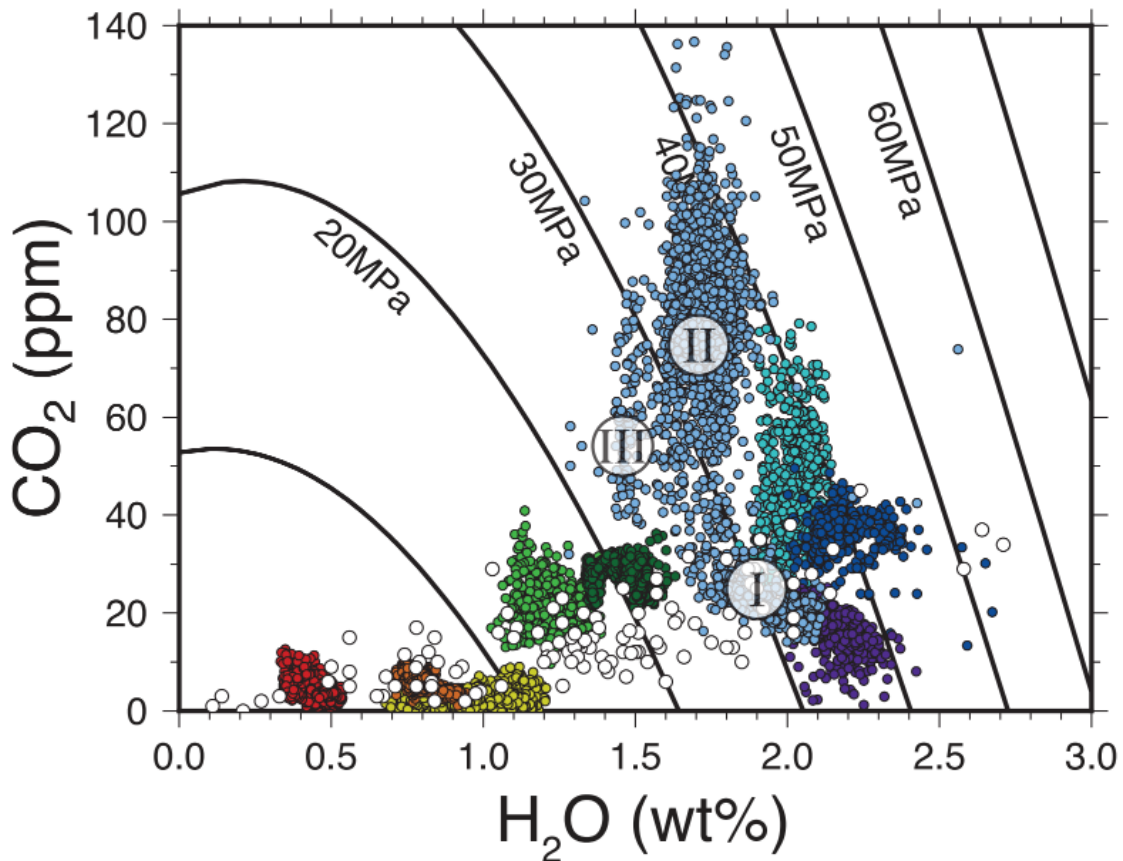
Figure 7. Volatile concentrations from the clast shown in Fig. 1 compared to results from a previous study (Watkins et al., 2017). The clast shown in Fig. 1 is exemplary of the key features seen in other clasts, including a CO_2-H_2O anti-correlation (Domain I) as well as highly variable CO_2 at fixed H_2O (Domains II and III).

4.3.1. Cooling rates

The volatile contents and cooling rates from the Fig. 1 pyroclast are shown in Fig. 8. The first thing to notice is that the CO_2-H_2O relationships are not sensitive to analytical spot size; the area maps measured by conventional FTIR (left panels) yield essentially the same results as a high-resolution transect measured by synchrotron FTIR (right panels). For cooling rates, the vast majority of spots analyzed (92%) give $Q > 10$ K/s. These high Q values are consistent with rapid air quench (Zhang et al., 2000), and suggest that the pyroclast did not cool slowly in the subsurface before being excavated during the eruption. It is noteworthy that the cooling rates do not increase systematically from core to rim as might be expected based upon thermal diffusion principles, suggesting that a single rapid quench applies to the clast as a whole. About 8% of the spots analyzed yield anomalously low cooling rates that we attribute to analytical artifacts related to the infrared beam intersecting vesicles, as discussed in Section 4.2. When we conservatively discard those data points with $Q < 25$ K/s, the results do not change either the general patterns or the details of the CO_2-H_2O distributions within the pyroclast, as shown further below in S4.3.4 where this 'Q-filter' is used as part of an argument against analytical artifacts contributing to sharp variations in dissolved CO_2.
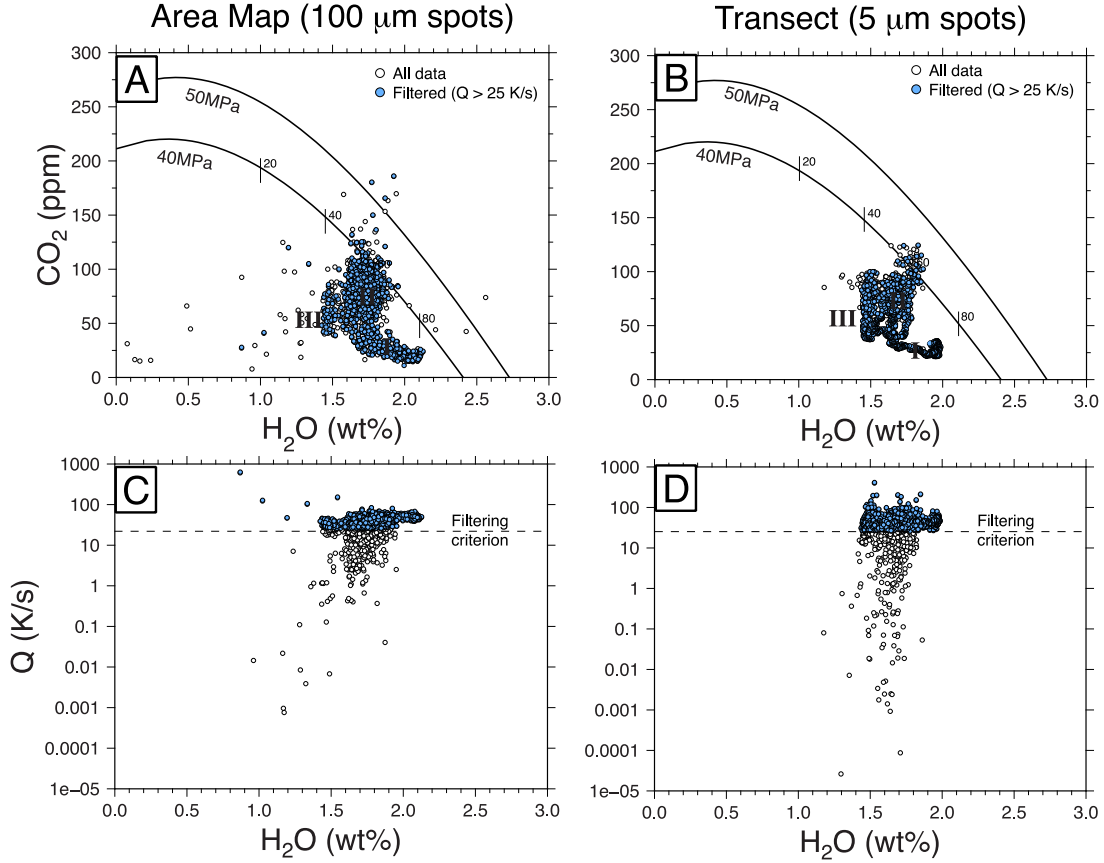
Figure 8. Volatile concentration data retrieved from the clast shown in Fig. 1. (a) The different textural domains have distinct volatile concentrations. The data are separated according to the Q-filter based upon experimental results (Fig. 5). (b) The high-resolution transect (5 μm spots) through the three domains indicates that overall results are independent of analytical spatial resolution. Panels (c) and (d) show that most of the cooling rates retrieved from the sample are consistent with air quench. Spots that yield low Q values (< 25 K/s) are treated with caution owing to possible analytical artifacts.

4.3.2 Vesicle relaxation timescales

When ash sinters in a static experiment, the interstices between ash particles have irregular shapes that relax over time to a spherical shape (Fig. 4). Under these conditions, the timescale for vesicle relaxation takes a similar form to the timescale for ash sintering (cf. Gardner et al., 2017):

$$\tau_v \sim \frac{\eta\,L}{\sigma} \tag{3}$$

18

where the characteristic lengthscale (*L*) is the vesicle radius. This relation states that small vesicles relax more quickly than larger vesicles.

One of the most striking observations in Fig. 1 is the presence of sharp-tipped, elongate vesicles that are small, on the order of 1x10 microns. Given a surface tension σ = 0.22 N m^{-1} and melt viscosity η = 6.3x10^6 Pa s (corresponding to 800°C and 1.5 wt% H$_2$O), the vesicle relaxation time is only ~3-30 s. However, this can be regarded as a minimum estimate for two reasons. First, we observe elongate, sharp-tipped vesicles persisting after 15 minutes of sintering in our fine ash experiments, and after 7 hours in our coarse ash experiments. The long timescale in the coarse ash experiments is attributable, in part, to higher viscosity, but the melt in those experiments should be fully hydrous within the first hour or so of sintering. Second, in a natural conduit system, the melt is likely to be undergoing shear deformation, especially along the conduit margins where obsidian pyroclasts are thought to form (Newman et al., 1988; Tuffen et al., 2003; Gonnermann and Manga, 2003; Gardner et al., 2017). Shear deformation would inhibit the relaxation of vesicle shapes and would also promote the formation of high aspect ratio vesicles. We therefore conclude that the scaling relation of Eq. 3 may, if anything, severely underestimate the longevity of elongate, cuspate vesicles and should be used with appropriate caution.

4.3.3 Sintering timescales

If true that Mono Craters obsidian pyroclasts formed by ash sintering, they would be categorized as fully sintered, high-density glasses with relatively low porosity. It is difficult to estimate the initial particle size from the natural pyroclasts because sintering quickly destroys individual grain boundaries as well as the initial distribution of interstitial gas or vesicles (Fig. 4). If they consist of sintered fine particles (<10 microns), they could have densified within minutes at magmatic temperatures. If instead they consist of sintered coarse particles (>100 microns), it could take hours for them to have sintered and densified. We have not collected or analyzed co-genetic ash from the deposit but there is probably a wide range of particle sizes, including fine ash that can quickly sinter together larger particles, perhaps as manifested by the dark suture zones in Fig. 1. Based on limited information, we speculate that the different domains of the pyroclasts could have sintered

19

within tens of seconds, and then each domain could have densified at its own rate depending on particle size.

4.3.4 Diffusion timescales

Gradients in dissolved H_2O and CO_2 can be used to obtain diffusion timescales that are more precise than timescales obtained from scaling relations. To better resolve these gradients, we measured a high-resolution synchrotron FTIR transect across the three domains. The results bring into clearer view the information obtained from area maps: H_2O gradients are relatively smooth whereas those for CO_2 are remarkably sharp in some places (Fig. 9).
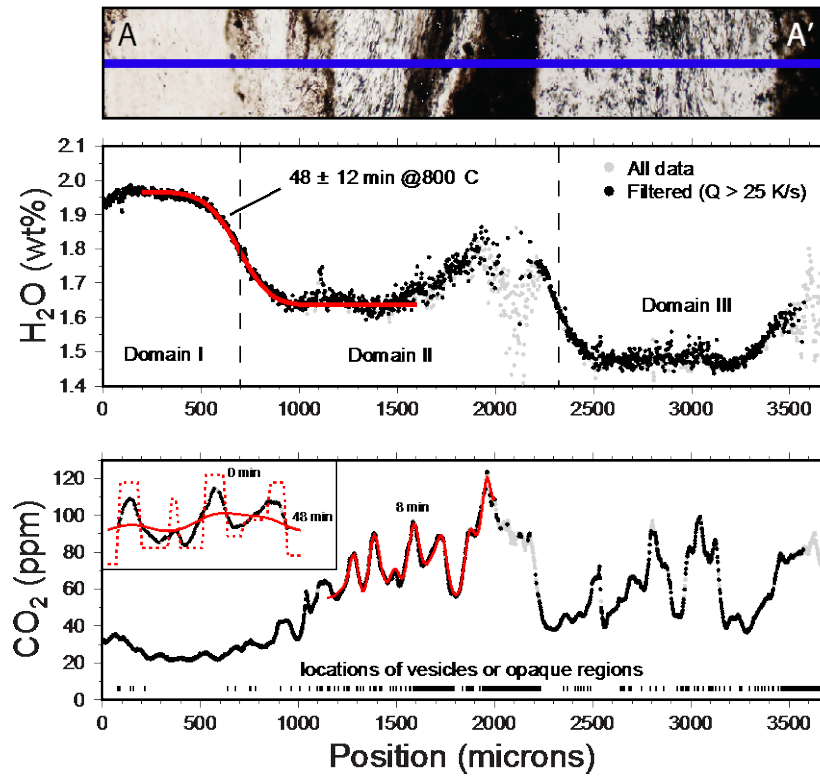
Figure 9. Synchrotron FTIR transect of H_2O and CO_2. Diffusion modeling of H_2O indicates that the high-H_2O (domain I) and low-H_2O (domain II) parts of the clast were juxtaposed within about 48 minutes of the eruptive quench. Diffusion modeling of the CO_2 profile suggests a much shorter timescale, on the order of 10 minutes, for assembly of the pyroclast; the inset shows how 48 minutes of diffusion creates smooth gradients that do not fit the data.

The sharp CO_2 peaks warrant some discussion. Because of concerns arising from the 5 μm beam intersecting vesicles, we applied the Q filter derived from our sintering experiments. Data points with Q values <25 K/s are shown as grey and are flagged as potentially underestimating the true dissolved volatile contents. Qualitatively, removal of

20

these data points does not affect the amount of diffusive relaxation that appears to have occurred. Furthermore, because the CO_2 peaks are much broader than either the analytical spot size or the average width of vesicles housed within the clast, and also because there is not a clear correspondence between the CO_2 peaks and the location of vesicles or opaque regions of the clast (Fig. 9b), we do not think they are artifacts of the analysis. These observations instill confidence that the gradients chosen for CO_2 diffusion modeling yield meaningful diffusive homogenization timescales.

In our approach to diffusion modeling, we try to identify chemical gradients with clearly definable initial conditions. The H_2O concentration profile across domains I and II in Fig. 1, for example, is a good target because there is a homogeneous low-H_2O region juxtaposed against a homogeneous high-H_2O region. To estimate how long H_2O was diffusing from high- to low-concentration, it is necessary to make a few simplifying assumptions. First, because the sample is a thin wafer, we acknowledge that we have information on chemical gradients in only two dimensions. Second, we assume that domains I and II had uniformly high-H_2O and low-H_2O contents, respectively, before being juxtaposed instantaneously without subsequent deformation. Third, we assume $T = 800°C$ based upon previous estimates of melt temperature from Fe-Ti oxide thermometry at Mono Craters (Carmichael et al., 1966). It is possible, however, that the pyroclast formed at lower temperatures, after the Fe-Ti oxides crystallized. We also assume $P = 40$ MPa, but the choice of pressure is not particularly important as it has a minor effect on diffusion coefficients. Lastly, we use fixed concentration boundary conditions, which is justified on the basis that the H_2O concentration profile is flat at both the low- and high-H_2O ends. Because the diffusivity of water depends on water concentration, we solve the 1D diffusion equation numerically using finite differences:

$$\frac{\partial^2 C_w}{\partial t^2} = \frac{\partial}{\partial x}\left(D_{H_2O}\frac{\partial C_w}{\partial x}\right) \qquad (4)$$

where D_{H_2O} depends on water concentration (Zhang et al., 2007). The model profile is compared to the measured data in Fig. 9, and the best-fit gives a timescale of about 48±12 min at 800°C.
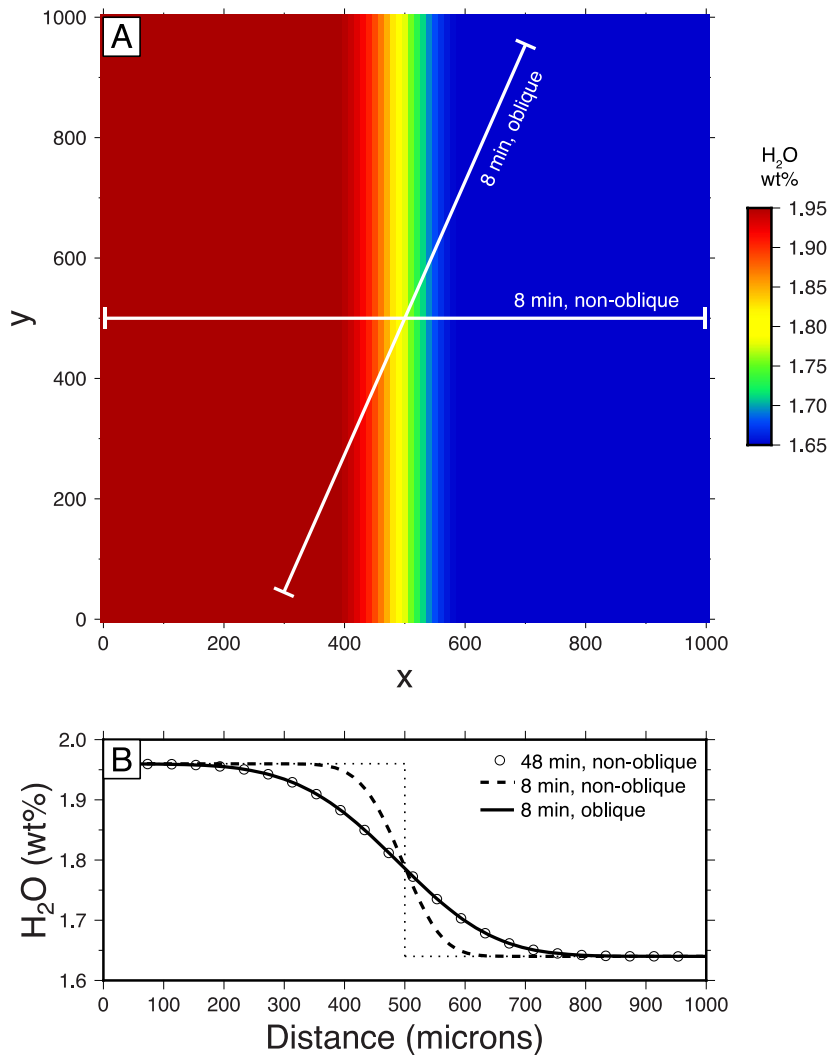
21

The CO_2 profile is not quite as amenable to a simplified diffusion model because of the sharp peaks and ambiguity in how to set up the initial concentration profile. The boundary conditions are also somewhat problematic because the concentration profile doesn't flatten out anywhere within the measured domain, and diffusion from one peak affects the neighboring peak. Nevertheless, we chose a representative segment of the profile and solved numerically the 1D diffusion equation using no flux boundary conditions:

$$\frac{\partial^2 C_w}{\partial t^2} = \frac{\partial}{\partial x}\left(D_{H_2O}\frac{\partial C_w}{\partial x}\right); \quad \frac{\partial C}{\partial x} = 0 \text{ at the boundaries} \tag{5}$$

where D_{CO_2} depends on dissolved H_2O (assumed to be a constant 1.7 wt%). The model was applied to a 1000 μm section of the profile in domain II and yields a timescale of ~ 8 minutes. Qualitatively, it appears that the CO_2 in domain I was partially homogenized prior to the diffusive homogenization that took place in domains II and III. Regardless of how one defines the initial concentration profile or boundary conditions of the model, the inescapable conclusion is that the sharp peaks in CO_2 with characteristic width of about 100 μm are much shorter-lived than allowed by the 48 minutes inferred from the H_2O profile (see inset to Fig. 9).

The difference in diffusion times recorded by H_2O and CO_2 can be reconciled in one of three ways: (1) diffusive exchange at lower temperature yields diffusion times for H_2O and CO_2 that converge to a value of about 10 hours at 600°C; (2) H_2O diffusion between the domains while small-scale CO_2 heterogeneities are continuously introduced, perhaps by flushing of a CO_2-rich vapor through a porous and permeable melt or ash matrix; (3) the H_2O diffusion time is overestimated because the thin section was not cut perpendicular to the concentration gradients. Scenario (1) is problematic because melt viscosity would be so high at 600°C that the timescale for ash sintering would be 80 to 800 hours for fine and coarse ash, respectively, which is beyond the eruption timescale. Scenario (2) is problematic because the porosity decreases rapidly and vesicles become isolated early during the sintering process, as demonstrated by our experiments. To test the viability of scenario (3), we constructed a 2D diffusion model (Fig. 10), allowed H_2O to diffuse for 8 minutes, and then extracted model 1D transects that were oriented at an

22

angle to the concentration gradient. Fig. 10 shows that an apparent diffusion time of 48 minutes can realistically be obtained by sampling a transect that is oblique to a concentration gradient produced by only 8 minutes of diffusion.

Figure 10. (a) 2D diffusion modeling of H_2O in rhyolite melt at 800°C was used to assess whether anomalously long diffusion times could be an artifact of slicing the clast at an oblique angle to the diffusion profile. (b) 8 minutes of H_2O diffusion can indeed produce an apparent diffusion time of 48 minutes.

4.3.5 Summary

The different timescales archived within obsidian pyroclasts provide complementary information. The self-consistent picture that emerges is that the clast shown in Fig. 1 was assembled by sintering of fine ash particles at high temperature (~800°C) within just a few minutes of the eruptive quench. The high temperature is required to sinter ash particles faster than the timescales retrieved by the volatile diffusion profiles and is also required to

23

explain the fast cooling rate across the glass transition temperature. The short timescale of a few minutes is sufficient to sinter fine ash at 800°C and is required to explain the preservation of small, sharp-tipped vesicles that would otherwise quickly relax to a rounded shape.

4.4 Implications for degassing models

Volatile concentrations in volcanic glasses from Mono Craters exhibit CO_2/H_2O ratios that are higher than would be expected from either closed- or open-system degassing of a single parental melt (Newman et al., 1988). This observation led to the idea that elevated CO_2 concentrations could be due to slow diffusion of CO_2 into vapor bubbles during magmatic ascent (Gonnermann and Manga, 2005), or continuous flushing of CO_2-rich vapor from a deep-seated source through the shallow magmatic system (Rust et al., 2004), or a combination of these two processes (Yoshimura and Nakamura, 2011).

Watkins et al. (2017) suggested that the association of sharp-tipped vesicles in areas of high dissolved CO_2 could constitute evidence for CO_2 flushing. Our experimental results corroborate this interpretation by showing that the timescales for ash sintering and vesicle relaxation are consistent with the timescales recorded by H_2O and CO_2 concentration gradients. Additional inferential evidence comes from the H_2O-CO_2 anticorrelation exhibited by roughly half the eight pyroclasts analyzed so far. Such an anti-correlation is the opposite of what one would expect from simple degassing but is consistent with the juxtaposition of ash/melt that has partially equilibrated with two different vapor compositions at a given depth within the system. We agree with Caricchi et al. (2018) that the exsolution of CO_2-rich fluids from deep-seated magma bodies and subsequent flushing of these fluids through shallow magmas may be a widespread and fundamental process in crustal magmatic systems. We show, however, that the evidence for CO_2-flushing as recorded by pyroclasts is short-lived and can quickly become obscured in the rock record.

V. Conclusions

Obsidian pyroclasts from Mono Craters, California, record a complex history of melt fragmentation, ash sintering, and vapor-melt exchange during magma ascent. The preservation of short-lived features such as cuspate vesicles and small-scale (~100 μm)

heterogeneities in dissolved volatiles motivated an experimental investigation into the nature of chemical exchange between vapor and melt during ash sintering.

We carried out rhyolite ash sintering experiments in the presence of a mixed CO_2-H_2O vapor using both fine ash (1-10's of microns) and coarse ash (10's to 100's of microns). The timescale for ash sintering and vesicle relaxation depends on melt viscosity. If diffusion of water is sufficiently fast, the melt viscosity can be calculated using the known solubility of water and the appropriate temperature and pressure. Addition of CO_2 to the system lowers the solubility of H_2O and increases viscosity to prolong the time required for ash sintering and vesicle relaxation. The timescale for sintering also depends on particle size. In fine ash experiments, the textural evolution takes place over about 30 minutes. After 7 minutes, the ash is barely sintered together and vesicles remain sharp-tipped. With time, the porosity decreases, the vesicles relax to a spherical shape, and after 30 minutes the ash is more-or-less fully sintered. In our coarse ash experiments, the ash is barely sintered after 45 minutes and subsequently undergoes a similar textural evolution as the fine ash experiments but over a longer time - on the order of a few hours. In both sets of experiments, vesicle relaxation to spherical shapes takes longer than estimated by scaling relations.

The experimental results support the interpretation that natural pyroclasts can form by ash sintering and record evidence for CO_2 flushing. For example, a diffusion timescale of ~8 minutes retrieved from modeling of H_2O and CO_2 concentration gradients was shown to be long enough for sintering to have occurred, yet short enough for vesicles to have not relaxed to a spherical shape. A CO_2-H_2O anticorrelation within pyroclasts and a relationship between sharp-tipped vesicles and high dissolved CO_2 concentrations is taken as evidence that CO_2 flushing from a deeper magmatic was involved in the eruption (Fig. 11). Whether or not the introduction of this vapor could have acted as an eruption trigger will require analysis of some of the earliest erupted deposits in the sequence.
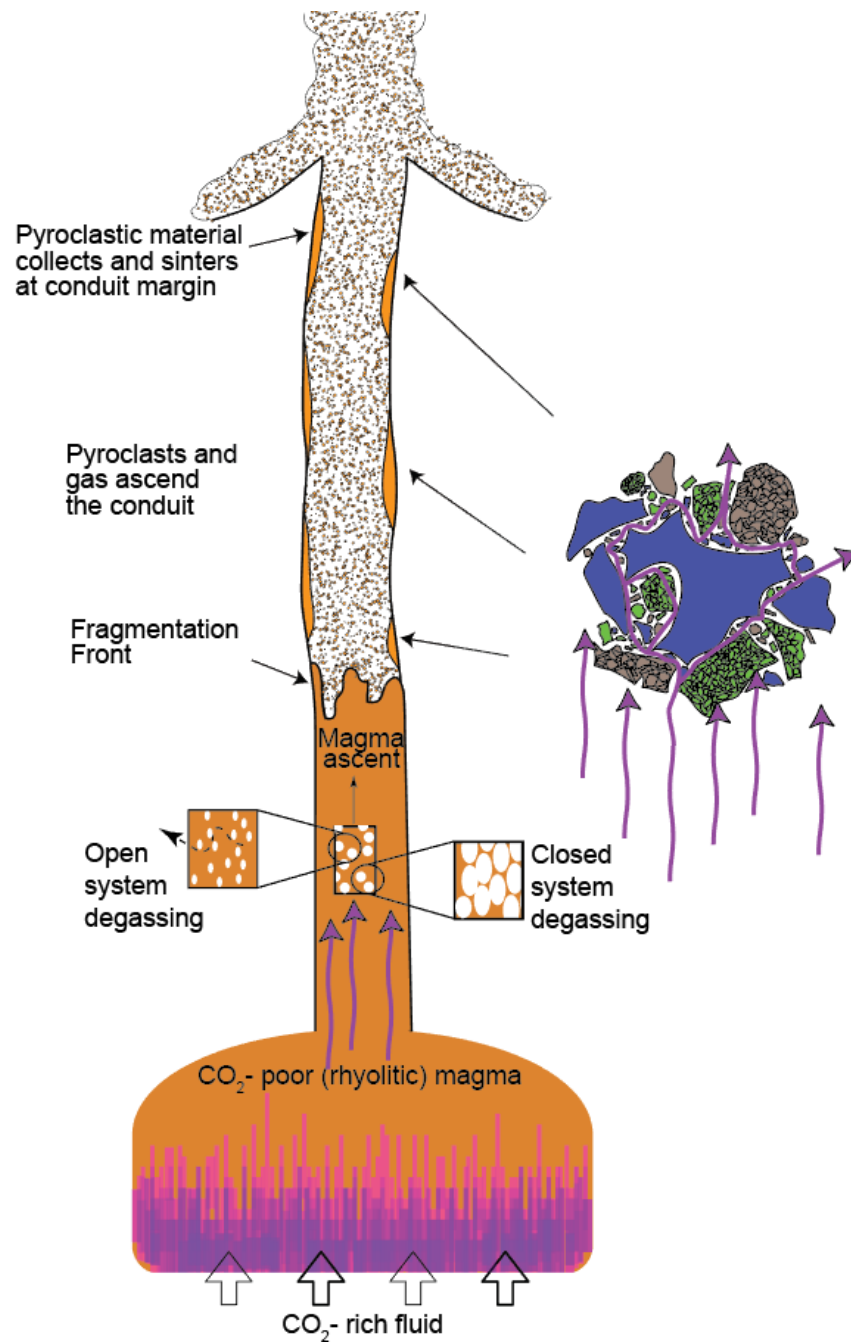
Figure 11. Schematic of conduit processes at Mono Craters, CA. As ash sinters, CO_2 from a deeper magmatic source is trapped between particles during sintering. Modified from Gardner et al. (2017) and Yoshimura and Nakamura (2011).

REFERENCES CITED

Bagdassarov N, Dorfman A, Dingwell DB (2000) Effect of alkalis, phosphorus, and water on the surface tension of haplogranite melt. Am Mineral 85:33–40

Barnes JD, Prather TJ, Cisneros M, Befus K, Gardner JE, Larson TE (2014) Stable chlorine isotope behavior during volcanic degassing of H_2O and CO_2 at Mono Craters, CA. Bull Volcanol 76:1–13

Behrens H, Tamic N, Holtz F (2004) Determination of the molar absorption coefficient for the infrared absorption band of CO_2 in rhyolitic glasses. Am Mineral 89:301–306

Carmichael IS (1966) The iron-titanium oxides of salic volcanic rocks and their associated ferro-magnesian silicates. Contrib Mineral Petrol 14:36–64

Caricchi L, Sheldrake, TE, Blundy, J (2018) Modulation of magmatic processes by CO_2 flushing. Earth Plane Sci Lett 491:160-171

Castro JM, Bindeman IN, Tuffen H, Schipper CI (2014) Explosive origin of silicic lava: Textural and δD-H_2O evidence for pyroclastic degassing during rhyolite effusion. Earth Planet Sci Lett 405:52–61

Dobson PF, Epstein S, Stolper EM (1989) Hydrogen isotope fractionation between coexisting vapor and silicate glasses and melts at low pressure. Geochim Cosmochim Acta 53: 2723–2730

Dufek J, Manga M, Patel A (2012) Granular disruption during explosive volcanic eruptions. Nature Geosci 5:561–564

Eichelberger JC, Carrigan CR, Westrich HR, Price RH (1986) Non-explosive silicic volcanism. Nature 323:598–602

Gardner JE, Llewellin EW, Watkins JM, Befus KS (2017) Formation of obsidian pyroclasts by sintering of ash particles in the volcanic conduit. Earth Planet Sci Lett 459:252–263

Gonnermann HM, Manga M (2003) Explosive volcanism may not be an inevitable consequence of magma fragmentation. Nature 426:432–435

Hess KU, Dingwell DB (1996) Viscosities of hydrous leucogranitic melts: a non-Arrhenian model. Am Mineral 81:1297–1300

Hui H, Zhang Y (2007) Toward a general viscosity equation for natural anhydrous and hydrous silicate melts. Geochim Cosmochim Acta 71:403–416

Liu Y, Zhang Y, Behrens H (2005) Solubility of H_2O in rhyolitic melts at low pressures and a new empirical model for mixed H_2O-CO_2 solubility in rhyolitic melts. J Volcanol Geotherm Res 143: 219–235

Martel C, Iacono-Marziano G (2015) Timescales of bubble coalescence, outgassing, and foam collapse in decompressed rhyolitic melts. Earth Planet Sci Lett 412:173–185

McIntosh IM, Llewellin EW, Humphreys MCS, Nichols ARL, Burgisser A, Schipper CI, Larsen JF (2014) Distribution of dissolved water in magmatic glass records growth and resorption of bubbles. Earth Plan Sci Lett 401:1-11

Newman S, Stolper EM, Epstein S (1986) Measurement of water in rhyolitic glasses: calibration of an infrared spectroscopic technique. Am Mineral 71:1527–1541

Newman S, Epstein S, Stolper EM (1988) Water, carbon dioxide, and hydrogen isotopes in glasses from the ca. 1340 AD eruption of the Mono Craters, California: Constraints on degassing phenomena and initial volatile content. J Volcanol Geotherm Res 35:75–96

Rust AC, Cashman KV, Wallace PJ (2004) Magma degassing buffered by vapor flow through brecciated conduit margins. Geology 32:349–352

Rust AC, Cashman KV (2007) Multiple origins of obsidian pyroclasts and implications for changes in the dynamics of the 1300 B.P. eruption of Newberry Volcano, USA. Bull Volcanol 69:825–845

Taylor BE, Eichelberger JC, Westrich HR (1983) Hydrogen isotopic evidence of rhyolitic magma degassing during shallow intrusion and eruption. Nature 306:541–545

Tuffen H, Dingwell DB, Pinkerton, H (2003) Repeated fracture and healing of silicic magma generate flow banding and earthquakes? Geology 31:1089–1092

Wadsworth FB, Vasseur J, von Aulock FW, Hess KU, Scheu B, Lavallée Y, Dingwell DB (2014) Nonisothermal viscous sintering of volcanic ash. J Geophys Res Solid Earth 119:8792–8804

Wadsworth FB, Vasseur J, Llewellin EW, Schauroth J, Dobson KJ, Scheu B, Dingwell DB (2016) Sintering of viscous droplets under surface tension. Proc Roy Soc A 472:20150780

Watkins JM, Gardner JE, Befus KS (2017) Nonequilibrium degassing, regassing, and vapor fluxing in magmatic feeder systems. Geology 45:183–186

Yoshimura S, Nakamura M (2010) Chemically driven growth and resorption of bubbles in a multivolatile magmatic system. Chem Geol 276:18–28

Yoshimura S, Nakamura M (2011) Carbon dioxide transport in crustal magmatic systems. Earth Plan Sci Lett 307:470-478

Yoshimura S, Nakamura M (2013) Flux of volcanic CO_2 emission estimated from melt inclusions and fluid transport modelling. Earth Plan Sci Lett 361:497-503

Zhang Y, Belcher R, Ihinger PD, Wang L, Xu Z, Newman S (1997) New calibration of infrared measurement of dissolved water in rhyolitic glasses. Geochim Cosmochim Acta 61:3089–3100

Zhang Y, Xu Z, Behrens H (2000) Hydrous species geospeedometer in rhyolite: improved calibration and application. Geochim Cosmochim Acta 64:3347–3355

Zhang Y, Xu Z, Zhu M, Wang H (2007) Silicate melt properties and volcanic eruptions. Rev Geophys 45:1–27